


Emergent Macroscopic Bistability Induced by a Single Superconducting Qubit

Riya Sett^{1,*}, Farid Hassani¹, Duc Phan¹, Shabir Barzanjeh^{1,2}, Andras Vukics^{3,†} and Johannes M. Fink^{1,‡}

¹*Institute of Science and Technology Austria, 3400 Klosterneuburg, Austria*

²*Institute for Quantum Science and Technology, University of Calgary, Calgary, Alberta T2N 1N4, Canada*

³*HUN-REN Wigner RCP, P.O. Box 49, Budapest, 1525, Hungary*

 (Received 28 October 2022; revised 5 October 2023; accepted 22 December 2023; published 16 February 2024)

The photon blockade breakdown in a continuously driven cavity QED system has been proposed as a prime example for a first-order driven-dissipative quantum phase transition. However, the predicted scaling from a microscopic behavior—dominated by quantum fluctuations—to a macroscopic one—characterized by stable phases—and the associated exponents and phase diagram have not been observed so far. In this work we couple a single transmon qubit with a fixed coupling strength g to a superconducting cavity that is *in situ* bandwidth κ tunable to controllably approach this thermodynamic limit. Even though the system remains microscopic, we observe its behavior becoming increasingly macroscopic as a function of g/κ . For the highest realized g/κ of approximately 287, the system switches with a characteristic timescale as long as 6 s between a bright coherent state with approximately 8×10^3 intracavity photons and the vacuum state. This exceeds the microscopic timescales by 6 orders of magnitude and approaches the perfect hysteresis expected between two macroscopic attractors in the thermodynamic limit. These findings and interpretation are qualitatively supported by neoclassical theory and large-scale quantum-jump Monte Carlo simulations. Besides shedding more light on driven-dissipative physics in the limit of strong light-matter coupling, this system might also find applications in quantum sensing and metrology.

DOI: [10.1103/PRXQuantum.5.010327](https://doi.org/10.1103/PRXQuantum.5.010327)

I. INTRODUCTION

Quantum phase transitions (QPTs), both first order and second order [1], have been at the forefront of physics research for half a century. The original idea of QPTs as abrupt shifts in the (pure) *ground state* of closed quantum systems as a function of a control parameter applied mostly to condensed matter physics. Dissipative quantum phase transitions (DPTs) occurring in the (in general, mixed) *steady state* of open quantum systems [2–12], however, broadened the scope of phase transitions to encompass mesoscopic systems and later even microscopic systems, where the interaction with the environment essentially affects the system dynamics. A DPT was first realized experimentally in a Bose-Einstein condensate interacting

with a single-mode optical cavity field [13], and DPTs are increasingly relevant to today’s quantum science and technology [14–17].

In view of this success, it is remarkable that in recent years yet another phase-transition paradigm could emerge, namely, *first-order* dissipative quantum phase transitions. A first-order phase transition means that two phases can coexist in a certain parameter region, such as water and ice at 0 °C for a certain range of free energy. Coexistence of phases in the quantum steady state seems paradoxical, since the steady-state plus normalization conditions for the density operator constitute a linear system of equations that admits only a single solution. That is, given the Liouvillian superoperator \mathcal{L} for the Markovian evolution of the system, there exists only a single normalized density operator ρ_{st} that satisfies [18]

$$\mathcal{L}\rho_{\text{st}} = 0. \quad (1)$$

The resolution is that a single density operator can accommodate the mixture of two macroscopically distinct phases expressed as a ratio of the two components. In the water analogy, at 0 °C we could symbolically write

$$\rho_{\text{st}} = c\rho_{\text{water}} + (1 - c)\rho_{\text{ice}}, \quad (2)$$

*riya.sett@ist.ac.at

†vukics.andras@wigner.hu

‡jfink@ist.ac.at

Published by the American Physical Society under the terms of the [Creative Commons Attribution 4.0 International](https://creativecommons.org/licenses/by/4.0/) license. Further distribution of this work must maintain attribution to the author(s) and the published article’s title, journal citation, and DOI.

with c growing from 0 to 1 as the free energy is increased.

Recently, first-order dissipative quantum phase transitions have been found in various systems. One such platform is the clustering of Rydberg atoms described by Ising-type spin models [19–24] and realized experimentally [25–27]. Various other systems of ultracold atoms [28,29] and dissipative Dicke-like models [30,31] also exhibit signatures of a first-order DPT. Other platforms include (arrays of) nonlinear photonic or polaritonic modes [7,32–39], exciton-polariton condensates [40,41], and circuit QED [16,42–45]. In this work we observe and model the scaling and phase diagram of a first-order DPT in zero dimensions, i.e., for a single qubit strongly coupled to a single cavity mode.

II. PHOTON BLOCKADE BREAKDOWN

The Jaynes-Cummings (JC) model—one of the most important models in quantum science—describes the interaction between atoms and photons trapped in a cavity [46]. It is expressed by the Hamiltonian ($\hbar = 1$)

$$H_{\text{JC}} = \omega_{\text{R}} a^\dagger a + \omega_{\text{A}} \sigma^\dagger \sigma + ig (a^\dagger \sigma - \sigma^\dagger a) + i\eta (a^\dagger e^{-i\omega t} - a e^{i\omega t}), \quad (3)$$

with ω_{R} the angular frequency of the cavity mode with boson operator a , ω_{A} the angular frequency of the atomic transition with operator σ , g the coupling strength, η the drive strength, and ω the angular frequency of the drive. This model yields the prototype of an anharmonic spectrum in the strong-coupling regime, as demonstrated in cavity QED [47] and circuit QED [48], and with quantum dots in semiconductor microcavities [49]. Its strong anharmonicity at the single-photon level is the basis of the photon blockade effect [50,51], in analogy with Coulomb blockade in quantum dots or with polariton blockade [52]. Photon blockade means that an excitation cannot enter the JC system from a drive tuned in resonance with the bare resonator frequency, or similarly, a second excitation from a drive tuned to resonance with one of the single-excitation levels cannot enter the JC system.

This blockade is, however, not absolute, as it can be broken [53–57] by strong-enough driving due to a combination of multiphoton events and photon-number-increasing quantum jumps [58]. In an intermediary η range, in the time domain the system stochastically alternates between a blocked, *dim state* without cavity photons and a *bright state* in which the blockade is broken and the system resides in the highly excited quasi-harmonic part of the spectrum, resulting in a large transmission of drive photons. In phase space, this behavior results in a bimodal steady-state distribution

$$\rho_{\text{st}} = c\rho_{\text{bright}} + (1 - c)\rho_{\text{dim}}, \quad (4)$$

in analogy with Eq. (2), with c growing from 0 to 1 with increasing η . This effect has been demonstrated experimentally in a circuit QED system [43].

Bistability in the time domain or bimodality in phase space is, however, not sufficient evidence for a first-order phase transition. It is also necessary that the two constituents in the mixture equation (4) corresponding to the two states in the temporal bistable signal be macroscopically distinct as is the case in Eq. (2). It has been shown theoretically [53,58] that the photon blockade breakdown (PBB) effect has such a regime, i.e., a *thermodynamic limit*, where both the timescale and the amplitude of the bistable signal go to infinity, resulting in long-lived and macroscopically distinct dim and bright phases. Remarkably, this thermodynamic limit is a strong-coupling limit, defined as $g/\kappa \rightarrow \infty$, and is independent of the physical system size, i.e., the system remains the same JC system composed of two microscopic interacting subsystems. In this limit, the temporal bistability is replaced by hysteresis, where the state of the system is determined by its initial condition, since switching to the other state entails an infinite waiting time. The passage to the thermodynamic limit, i.e., the indefinite increase of g/κ has been termed “finite-size scaling” [58].

In this work, we demonstrate these additional criteria that clearly signify the observed physical effect as a first-order dissipative quantum phase transition. We demonstrate the finite-size scaling over 7 orders of magnitude towards the thermodynamic limit and extract the phase diagram of a first-order DPT in zero dimensions. We realize this experiment with a superconducting qubit strongly coupled to a bandwidth-tunable microwave cavity mode and find qualitative agreement with large-scale quantum-jump Monte Carlo (QJMC) simulations and neoclassical calculations of the phase boundaries.

III. EXPERIMENTAL IMPLEMENTATION

Our experimental setting incorporates a transmon qubit [59,60] placed at the antinode of the standing wave of a 3D copper cavity, as shown in Fig. 1(a), that can be flux tuned by application of a magnetic field via a millimeter-sized superconducting bias coil mounted at the outside cavity wall. The transmon qubit has maximum Josephson energy $E_{\text{J,max}}/h \approx 48$ GHz, charging energy $E_{\text{C}}/h \approx 382$ MHz, and a resulting maximum transition frequency $\omega_{\text{A}}/2\pi$ between its ground and first excited states of approximately 12.166 GHz. When the transmon ground state to first excited state transition is tuned in resonance with the cavity mode at $\omega_{\text{R}}/2\pi \approx 10.4725$ GHz, the directly measured coupling strength $g/2\pi$ between the single photon and the qubit transition is as high as 344 MHz, which is about only a factor of 3 below the so-called ultrastrong-coupling regime [61]. The relatively high absolute anharmonicity Δ_{an}/h between subsequent transmon

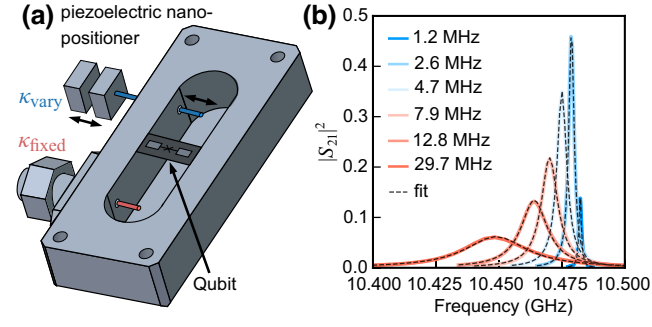


FIG. 1. Experimental realization. (a) Schematics of the experimental device consisting of a superconducting transmon qubit fabricated on a silicon substrate that is placed at the antinode of the fundamental mode of a 3D copper cavity. The cavity has a fixed-length port (red) and an *in situ* variable-length pin coupler port (blue). (b) Measured cavity transmission spectra with the qubit far detuned for different coupler positions (color coded) together with a fit to Eq. (5) (dashed lines) and the extracted $\kappa/2\pi$.

state transitions is approximately -418 MHz at this flux bias position.

The cavity has two ports, of which the input pin coupler position is fixed with an external coupling strength $\kappa_{\text{fixed}}/2\pi$ of approximately 500 kHz. The output coupler is attached to a cryogenic piezoelectric nanopositioner, which allows adjustment of the pin length extending into the cavity [62]. With this tunable coupler, the coupling strength can be varied *in situ* in a wide range, $\kappa_{\text{vary}}/2\pi \approx 20$ kHz to 30 MHz. The internal cavity loss at low temperature $\kappa_{\text{int}}/2\pi$ is approximately 600 kHz, which is achieved by electropolishing of the high-conductivity copper surface before cooldown to 10 mK in a dilution refrigerator.

All four scattering parameters are measured with a vector network analyzer to calibrate the measurement setup and the cavity properties when the qubit is far detuned from the cavity resonance. Figure 1(b) shows transmission measurements fitted with the scattering parameter S_{21} derived from the input-output theory of an open quantum system [63]:

$$S_{21} = \frac{\sqrt{\kappa_{\text{fixed}}\kappa_{\text{vary}}}}{\kappa/2 - i(\omega - \omega_{\text{R}})}. \quad (5)$$

From these fits, we extract all loss rates that add up to the total cavity linewidth $\kappa = \kappa_{\text{fixed}} + \kappa_{\text{vary}} + \kappa_{\text{int}}$, also indicated in Fig. 1(b).

Time-domain characterization measurements confirm that the qubit is Purcell limited and homogeneously broadened at the flux sweet spot [64], where the measured energy relaxation time $T_1 = 1/\gamma_1 \approx 0.5 \mu\text{s}$ and the coherence time $T_2 = (\gamma_1/2 + \gamma_\phi)^{-1} \approx 1 \mu\text{s}$, where γ_ϕ is the pure dephasing rate. When the qubit frequency is tuned far below the resonator frequency $\omega_{\text{A}}/2\pi \approx 6.083$ GHz by

application of an external magnetic field, the measured coherence times are $T_1 \approx 18.14 \mu\text{s}$ and $T_2 \approx 0.496 \mu\text{s}$, which we attribute to a higher Purcell limit due to the larger detuning as well as drastically increased flux noise sensitivity. On resonance $\omega_{\text{A}} = \omega_{\text{R}}$, where the following experiments were performed, the energy relaxation is therefore fully dominated by cavity losses. The measured vacuum Rabi peak linewidth changes with and without the qubit in resonance are in agreement with a small amount of flux-noise-induced dephasing expected at this flux bias position.

IV. BIMODALITY AND CHARACTERISTIC TIMESCALES

The photon blockade and its breakdown (PBB) most straightforwardly occur when the two interacting constituents are resonant, i.e., $\omega_{\text{A}} = \omega_{\text{R}}$. In this and the next section, we furthermore consider the case of driving the system on resonance: $\omega = \omega_{\text{R}}$. In contrast to the simplest case of a two-level atom [53,58], where this leads to a critical point, signifying a second-order DPT [53,55] (the so-called spontaneous dressed-state polarization [66–68]), in our experimental situation where at least three transmon levels are relevant, we still have bistability of the resonator intensity. In Ref. [43], an interpretation of this difference was given in terms of the spectrum of a three-level system strongly coupled to a harmonic oscillator mode, which we summarize in Fig. 2(a). In Appendix B, we further elaborate on this difference in the frame of an approximate neoclassical theory extended to the three-level atom case.

For low input powers corresponding to less than a single intracavity photon on average, we observe a vacuum-Rabi-split spectrum in transmission, as shown in Figs. 2(a) and 2(b) (blue line). No transmission peak is observed at the bare cavity frequency ω_{R} up to intermediate input drive strengths η . This means that a single photon—or even hundreds of photons at the chosen $g/\kappa = 39.1$ —are prevented from entering the cavity due to the presence of a single artificial atom.

This blockade is observed to be broken abruptly by further increasing the applied drive strength η , which is proportional to the square root of the applied drive power and the corresponding drive photon number. As η is increased by only a finite amount close to the PBB, the transmitted output power increases by 3 orders of magnitude at the bare resonator frequency, as shown in the red spectrum in Fig. 2(b). The central sharp peak in the transmission spectrum corresponds to a time-averaged measurement (determined by the resolution bandwidth chosen) of a cavity that is fully transparent for most of the integration time. This PBB effect can be attributed to the nonlinearity of the lower part of the JC spectrum, which is strongly anharmonic [48,69], while the higher-lying part of the spectrum has subsets that are closely harmonic over a certain range

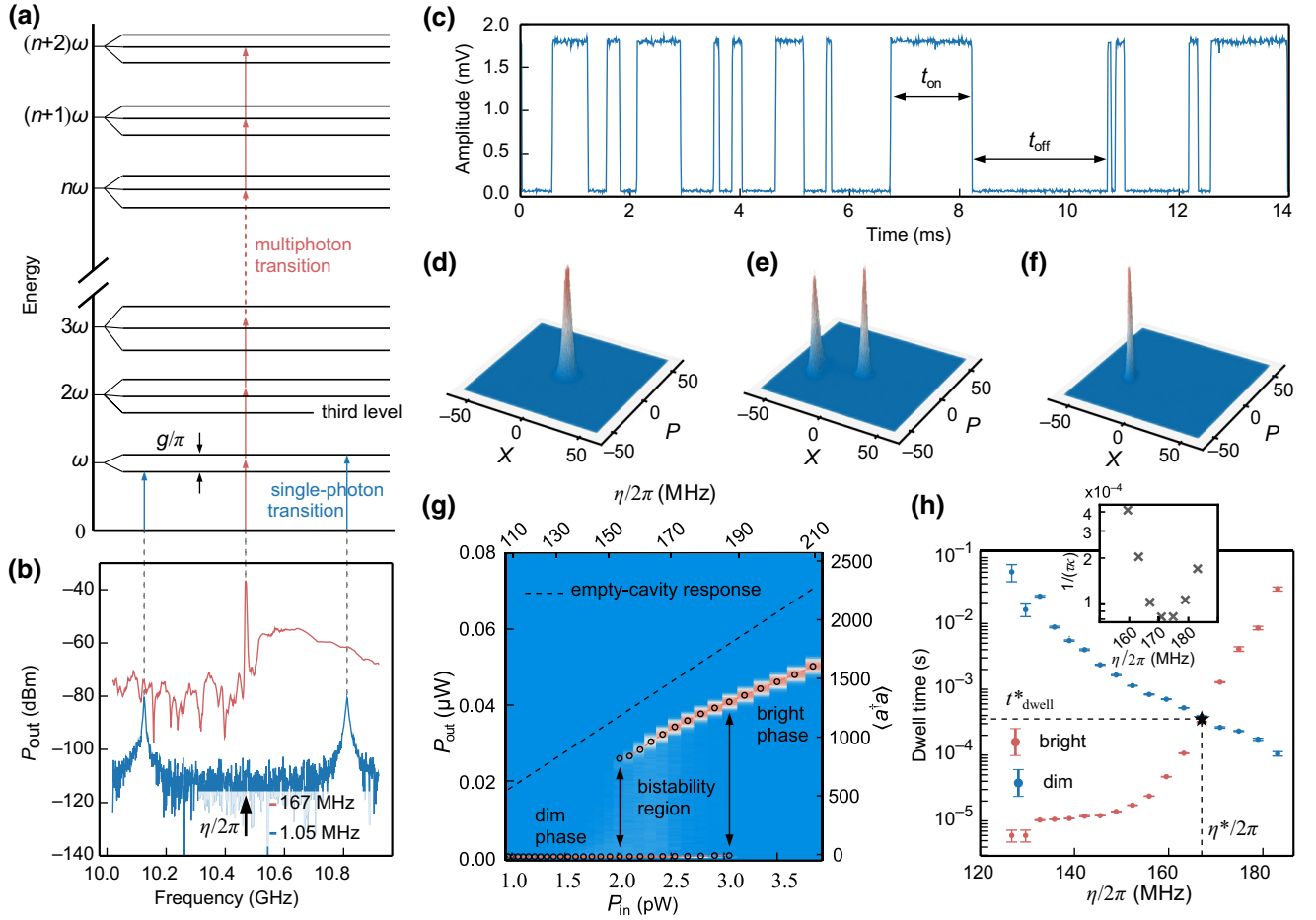


FIG. 2. Photon blockade breakdown measurements at $g/\kappa \approx 39.1$. (a) The Jaynes-Cummings ladder for a three-level atom illustrating the PBB effect in the frequency domain: single-photon (blue) and multiphoton transitions (red) are indicated according to the measured spectrum at the Rabi-splitting frequencies and near resonance, respectively. As indicated, the third atomic state causes a third subladder in the spectrum starting from the second rung, whose spacing is close to the bare-system frequency. This is a possible explanation for the PBB bistability persisting in the case of resonant driving. (b) Measured cavity transmission spectra for $\omega_A = \omega_R$ for two applied external drive strengths: 1.05 MHz, revealing a typical vacuum Rabi spectrum, and 167.01 MHz, where a sharp peak at ω_R is observed. (c) Measured cavity output bistability at $\omega = \omega_R$ in the time domain indicating the dwell times of the bright state (t_{on}) and the dim state (t_{off}). (d)–(f) Measured quadrature histograms (proportional to cavity Q functions convolved with amplifier noise) for the dim phase at $\eta/2\pi = 105$ MHz, for the bistable region with equal probability at 167 MHz, and for the bright phase at 210 MHz, respectively. (g) Measured histograms of the output power (arranged vertically and with probability color coded) as a function of input power. The maxima indicated by circles trace out a typical bistability curve; see Fig. 4(b). (h) Extracted average dwell times in the dim and bright states [Eq. (6)] as a function of η . The error bars represent the standard error that is extracted from five sections of the full dataset. The dwell time and drive strength corresponding to half-filling where $t_{\text{dwell}}^{\text{dim}} = t_{\text{dwell}}^{\text{bright}}$ are indicated with an asterisk. The inset shows the measured slow-switching eigenvalue $1/\tau$, from Eq. (7), in the unit of κ as a function of drive amplitude η close to half-filling [65].

of excitation numbers [70] and can hence accommodate a closely coherent state.

In the time domain, with η in the phase coexistence region, the PBB effect results in a bistable telegraph signal, where the system output alternates between a “dim” state, where the qubit-resonator system remains close to the vacuum state unable to absorb an excitation from the externally applied drive, and a “bright” state, where the system resides in an upper-lying, closely harmonic subset of the JC spectrum; see Fig. 2(c). The switches between these

two classical attractors are necessarily multiphoton events that are triggered by quantum fluctuations. This bistability was shown to be a finite-size precursor of what would be a first-order DPT in the thermodynamic limit ($g/\kappa \rightarrow \infty$) [58], where the bistability develops into perfect hysteresis: the system is stuck in the attractor determined by the initial condition as long as the control parameters are set in the transition domain [71].

To investigate this dynamics qualitatively, we record the real-time single-shot data of both quadratures of the

transmitted output field at the bare cavity frequency while applying a continuous-wave drive tone resonant with the bare cavity over a range of applied drive strengths. The transmitted radiation is first amplified with a high-electron-mobility transistor at 4 K, followed by a room-temperature low-noise amplifier, and then down-converted with an in-phase and quadrature mixer with appropriate intermediate frequency and finally digitized with a digitizer. The recorded data are then digitally low-pass filtered with appropriate resolution bandwidth and down-converted to 0 Hz to extract the time-dependent quadratures in voltage units. For example, in the case of $\kappa/2\pi = 8$ MHz, the recorded data are 2.88 s long and the final time resolution of the extracted quadratures is $2.5 \mu\text{s}$; see Fig. 2(c). The selection of an appropriate resolution bandwidth is critical for a number of reasons: (1) to successfully resolve frequent and sudden switching events caused by very short dwell times at high κ values, (2) to maintain a signal-to-noise ratio that allows one to clearly discriminate single-shot measurement events without averaging, and (3) to achieve a sufficient total measurement time to resolve long dwell times with the available memory.

From the resulting histograms in phase space [see Fig. 2(d)–2(f), which represent the scaled Husimi Q functions convolved with the added amplification chain noise photon number $n_{\text{amp}} \approx 9.2$], it can be deduced that for low drive strength the photon blockade is intact (dim phase) with the Q function being centered at the vacuum state. When the input drive strength is increased, the Q function becomes bimodal with decreasing weight of the dim state as described in Eq. (4). At high-enough η , only the bright coherent state is measured. Note that the transformation of the Q function and hence the steady-state density operator of the system as a function of η is continuous, yet a first-order phase transition with a well-defined coexistence region can occur.

A similar conclusion can be drawn from the output power histograms (color map) that trace out a typical bistability curve as shown in Fig. 2(g). The most likely output powers P_{out} and calculated equivalent intracavity photon numbers of the empty cavity driven on resonance $\bar{n}_{\text{cav}} = 4P_{\text{in}}\kappa_{\text{fixed}}/\hbar\omega_{\text{R}}\kappa^2$ as a function of applied input power P_{in} and resulting drive strength $\eta = \sqrt{\bar{n}_{\text{cav}}}\kappa/2$ are marked with circles. The vacuum, bistability, and bright regions are well defined. We find that the derivative of the bright solution obtained at high P_{in} deviates somewhat from the empty-cavity response measured when the qubit is far detuned (dashed line). For large g/κ values, this is more pronounced and we have observed that this can lead to secondary bistability regions at even higher powers for $g/\kappa \gtrsim 43$, which we believe to originate from the multilevel nature of the transmon qubit. In this work, we focus only on the bistability occurring at the lowest drive strength.

In Fig. 2(h) we show the measured dwell times of dim and bright states as a function of input power. The average dwell times at each input power are calculated as

$$t_{\text{dwell}}^{\text{dim}} = \frac{1}{N} \sum_{n=1}^N t_{\text{off},n}, \quad t_{\text{dwell}}^{\text{bright}} = \frac{1}{N} \sum_{n=1}^N t_{\text{on},n}, \quad (6)$$

and the threshold for one of the N switching events during the full measurement duration (with $2.5\text{-}\mu\text{s}$ resolution) is defined at half of the observed full amplitude for the lowest applied $\eta/2\pi \approx 140$ MHz where the bistability is fully developed. Note that in cases of low signal-to-noise ratio, e.g., for large κ or at high drive detunings shown later, we used a higher threshold that at least exceeds the variance of the output power of the dim state.

At low η there are only few switching events because the system remains in the dim state for long timescales. As η is increased to $\eta^*/2\pi \approx 167$ MHz the measured average dwell times cross at $t_{\text{dwell}}^{\text{dim}} = t_{\text{dwell}}^{\text{bright}} = t_{\text{dwell}}^* \approx 354 \mu\text{s}$. We call this the “half-filling point”, where it is equally likely for the system to be found in the dim state or the bright state, denoted by an asterisk in Fig. 2(h). For even higher drive strength, the system prefers to dwell in the bright state, i.e., we observe close to full resonator transmission for most of the time.

Finally, to complete the study of the breakdown process through the bistable cavity transmission, we define the overall characteristic timescale of the system as

$$\tau = \left(\left(t_{\text{dwell}}^{\text{dim}} \right)^{-1} + \left(t_{\text{dwell}}^{\text{bright}} \right)^{-1} \right)^{-1}, \quad (7)$$

see Table 1 in Ref. [58], since it governs the rate with which the system evolves into the appropriate steady-state mixture of the two attractors from an arbitrary initial state. This is the slowest characteristic timescale in the system that diverges in the thermodynamic limit. The unitless slow-switching eigenvalue of the time evolution of the system is the inverse of this characteristic timescale, $\lambda = 1/\tau\kappa$, whose dependence on η can be seen in the inset in Fig. 2(h). It shows the minimum $\lambda \ll 1$ close to the half-filling point in agreement with the predicted “slowing down” of the system dynamics [65].

V. FINITE-SIZE SCALING TOWARDS THE THERMODYNAMIC LIMIT

In the context of first-order DPTs, “macroscopic behavior” can be defined independently of experimental characteristics such as the signal-to-noise ratio or the resolution of a “macroscopic” detector. Rather, it is the concept of a thermodynamic limit that distinguishes a first-order DPT from temporal bistability. Whereas normally the thermodynamic limit of phase transitions is reached

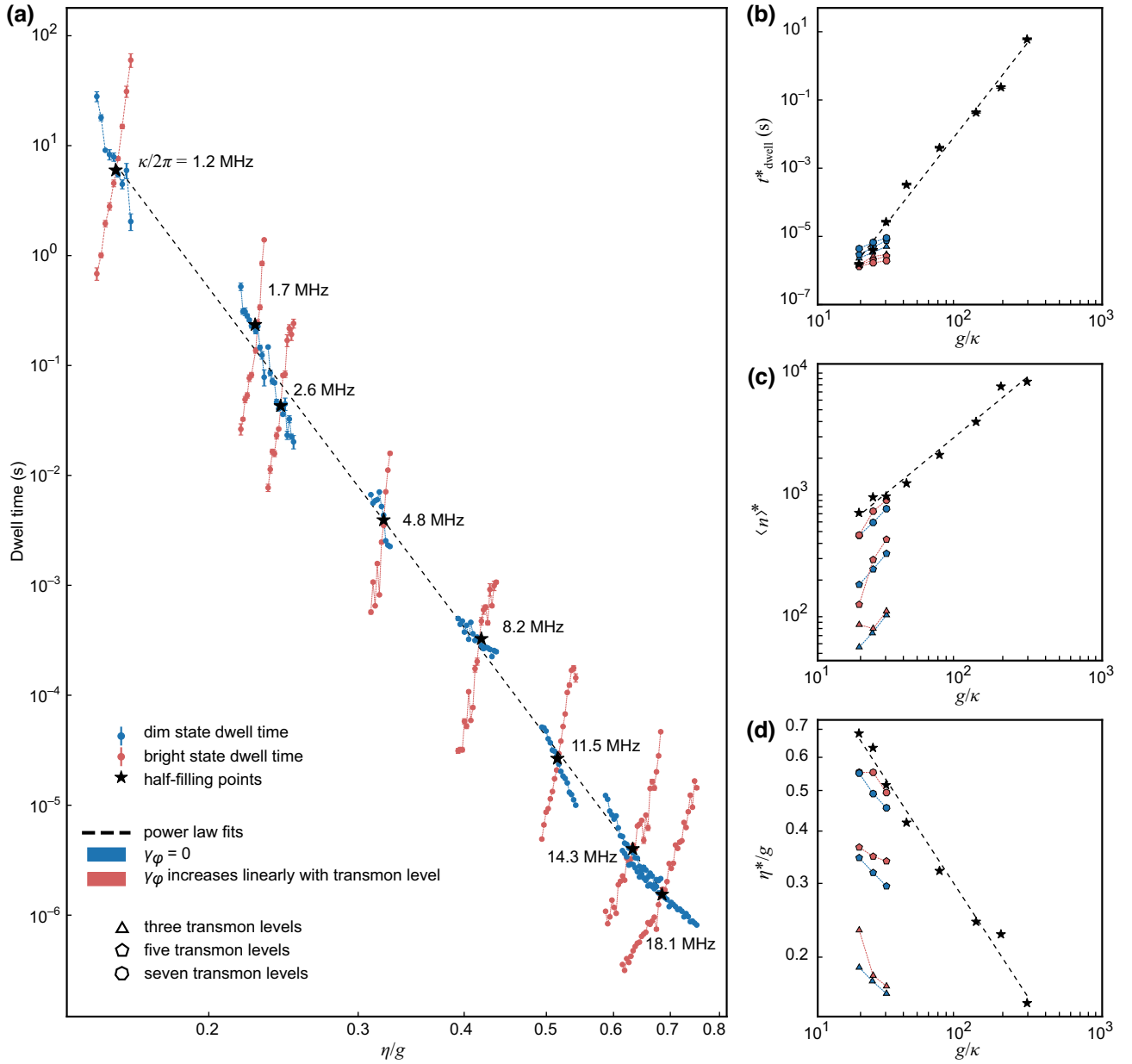


FIG. 3. Finite-size scaling towards the thermodynamic limit. (a) Measured dwell times in the dim state (blue) and the bright state (red) are shown as a function of η/g for different values of κ . Black stars denote half-filling values, where the probabilities of being in the dim state or the bright state are equal. The dashed line is a power law fit. The error bars represent the standard error that is extracted from at least three sections of the full dataset. (b)–(d) Measured scaling laws as a function of control parameter g/κ at half-filling (asterisks). Fitting the experimental data (dashed lines) yields the exponents $t_{\text{dwell}}^* \propto (g/\kappa)^{5.4 \pm 0.2}$ for the dwell time, $\langle n \rangle^* \propto (g/\kappa)^{0.96 \pm 0.05}$ for the average resonator photon number, and $\eta^*/g \propto (g/\kappa)^{-0.52 \pm 0.03}$ for the input drive strength. We compare the experimental values (stars) with those obtained from QJMC simulations (polygons with color code) for computationally manageable $\kappa = 11.5, 14.3,$ and 18.1 MHz. The simulations include three, five, or seven transmon levels both without transmon dephasing (light blue) and with dephasing increasing linearly with the level number (light red) with $\gamma_{\phi,1}/2\pi = 50$ kHz and $\gamma_1 = 0$. Details of the simulation are given in the main text and in Appendix A.

by increasing the system size (e.g., the number of particles), in the case of the PBB, it depends on the dynamical parameter g/κ . Moving towards the thermodynamic limit, $g/\kappa \rightarrow \infty$ has been termed “finite-size scaling” [58], along which a temporal bistability becomes a first-order

DPT with attractors of increasingly distinct intensity and dwell time, eventually leading to perfect hysteresis. In this limit, the initial state of the system determines which of the two possible coexisting states it will be frozen into.

While, in principle, the distinction between bright and dim attractors in terms of intensity and dwell time go to infinity in the thermodynamic limit, the drive power necessary to reach the bistability region is also expected to go to infinity. In the experiment, this would at some point put the system into an invalid state, e.g., by breaking the superconductivity of the transmon qubit. Nevertheless, in the present case, we demonstrate the predicted finite-size scaling over many orders of magnitude both in the dwell time and in intensity. With this we show—despite the underlying microscopic nature of the system—a truly macroscopic behavior. We also experimentally determine the finite-size scaling exponents of the characteristic time, corresponding drive strength, and intracavity photon number for this DPT.

In Fig. 3(a) we show the measured dwell times as a function of drive strength—similarly to Fig. 2(h)—for different $\kappa/2\pi$ values ranging from 1.21 to 18.1 MHz. For each κ value the dwell time in the dim state (blue symbols) decreases with increasing drive strength and that of the bright state (red symbols) increases until eventually the system is fully stabilized in the bright state. For each g/κ value, we define a single characteristic time of the process t_{dwell}^* at the drive strength η^* that leads to half-filling of the telegraph signal; see also Fig. 2(h).

Remarkably, for the largest realized value of g/κ (i.e., 287), the characteristic dwell time t_{dwell}^* reaches approximately 6 s. This exceeds the characteristic microscopic dissipation times of order κ^{-1} and T_2 by a factor of more than approximately 10^6 and is reminiscent of the emergence of two macroscopically distinct states with strongly suppressed transitions that require a cascade of quantum jumps [58]. This strong-coupling, high photon number limit where the effect of quantum fluctuations vanishes has been defined as the thermodynamic limit of such a finite-size zero-dimensional system [53].

Finite-size scaling also requires that the characteristic timescale and brightness scale as a function of g/κ , while the system remains self-similar, which in this case means that it keeps switching stochastically at a fixed filling factor. In Fig. 3(b) we plot the measured increase of t_{dwell}^* at filling 0.5 over a range of 7 orders of magnitude as a function of g/κ . The behavior follows a strong power law over the full range, and the fitted finite-size scaling exponent is $t_{\text{dwell}}^* \propto (g/\kappa)^{5.4 \pm 0.2}$. Similarly, the intracavity photon number of the bright state at half-filling increases nearly linearly with $\langle n \rangle^* \propto (g/\kappa)^{0.96 \pm 0.05}$, as shown in Fig. 3(c), and as a consequence the corresponding drive strength decreases with the square root, $\eta^*/g \propto (g/\kappa)^{-0.52 \pm 0.03}$, as shown in Fig. 3(d). Here the normalization of the drive amplitude with g is motivated by the two-level neoclassical theory, where the critical point appears at $\eta/g = 0.5$ for $\Delta = 0$.

The theoretical results (triangles, pentagons, and heptagons) shown in Figs. 3(b)–3(d) are taken from large-scale

numerical simulations performed with C++QED, a framework for simulating open quantum dynamics [72]. An adaptive version of the QJMC method is applied, where a single stochastic quantum trajectory is considered to correspond to a single experimental run [73]. The shown data are based on 64 CPU years of simulation time with a Hilbert space dimension of up to approximately 2^{15} (seven transmon levels and 3–5 times $\langle n \rangle^*$). Another computationally demanding aspect is that the required time step is set by the largest characteristic frequency (typically g or η) of the microscopic system (sampled with $1/\kappa$ to reduce data volume), whereas the total trajectory needs to cover many times t_{dwell} to obtain sufficient statistics of the macroscopic behavior. Together this limits the range of numerically accessible g/κ values to the lowest three values measured. For more details on how we model the system, examples of simulated quantum trajectories, and the impact of different transmon dephasing models, see Appendix A.

The observed photon number scaling exponent is about half of the analytical prediction of $\langle n \rangle^* \propto (g/\kappa)^2$; see Eq. (6) in Ref. [58]. This is not surprising since the two-level neoclassical theory does not yield quantitative agreement for the case with a multilevel transmon circuit. Numerical simulations for the lowest three g/κ values taking into account up to seven transmon levels [heptagons in Fig. 3(c)], agree with the measured linear exponent to within 15%. The absolute value of $\langle n \rangle^*$ also agrees well (blue) and is further improved when we include qubit dephasing of all transmon levels (red) due to flux noise with the measured $\gamma_\phi/2\pi \approx 50$ kHz for the lowest qubit transition; that is, as long as enough transmon levels are taken into account. In the case of just three transmon levels, the simulated value is about an order of magnitude smaller than the measured value. This highlights the importance and participation of multiple transmon levels in the dynamics of the system.

The dwell times and scaling shown in Fig. 3(b) are more robust with regard to the number of transmon levels but we observe a substantial deviation between the measured (5.4) and simulated scaling exponents in the range from 0.9 to 2.2. In Ref. [58], on the basis of a two-level model with finite detuning, the blink-off rate could be calculated from the rate of ladder-switching quantum jumps, and was found to be proportional to $\kappa/\langle n \rangle^*$, so the waiting time for a blink-off is $\langle n \rangle^*/\kappa$; therefore, it scales as g^2/κ^3 . The numerically determined timescale exponent in the same work was $\kappa t_{\text{dwell}}^* \propto (g/\kappa)^{2.2}$, which is very close to the analytical value.

The observed scaling exponent is significantly larger, which may be due to ultrastrong-coupling effects kicking in earlier than commonly expected, such as the counter-rotating terms not taken into account in the numerical simulations (for a numerical treatment of the Bloch-Siegert shift, see Ref. [74]) and the hybridization of decay channels [75,76], which can invalidate our approach of using

separate transmon and resonator decay channels in the master equation. Other potentially participating mechanisms could include transmon ionization [77] or dielectric surface loss saturation [78] that might further stabilize the system—in particular in the bright attractor—and thus reduce the blink-off probability. Taken together, these effects appear to be driving the system significantly faster to the thermodynamic limit compared with what would be expected from the standard Jaynes-Cummings model.

Importantly and irrespective of the origin of the unexpectedly strong scaling, we observe that the system is always able to relax to the vacuum state eventually—despite the continuous driving. This vacuum state is then stabilized for seconds by the presence of a single qubit, even for the highest drive strength corresponding to a photon number $\langle n \rangle$ of approximately 10^4 . In contrast to similarly looking fluorescence signals with dwell times on the order of seconds, which have been known in quantum science since the first electron-shelving experiments with single ions in Penning traps [79,80] due to long-lived metastable atomic states, in the present case the measured timescale exceeds all microscopic timescales by many orders of magnitude, i.e., the system is very deep in the macroscopic limit, which justifies its classification as a phase transition in a microscopic quantum system.

VI. PHASE DIAGRAM

The PBB phase transition has been predicted to exhibit an interesting phase diagram as a function of drive detuning $\Delta \equiv \omega - \omega_R = \omega - \omega_A$. From the neoclassical equations, valid for pure two-level qubit states and $\gamma_1 = \gamma_\phi = 0$ [81], the bistable region is expected only at finite detunings away from the critical point at $\Delta = 0$ [53,58]. This model can be extended with a third atomic level to provide a more realistic description of the transmon. For the extension, the population of the third level must be ignored, while we keep the coherences between all levels (for details, see Appendix B), which is a reasonable approximation given the anharmonicity of the transmon. Solutions to these models are shown in Figs. 4(a) and 4(b) for a two-level transmon and a three-level transmon, respectively. In the latter case, because of the very high order polynomials appearing in the solution, it is impractical to extract the full phase diagram; therefore, the multistable transmission curves are shown instead. The two-level and three-level cases are qualitatively different: the latter shows an asymmetry with respect to the $\Delta = 0$ point as well as multistability for negative detunings—this has not been observed experimentally. Importantly though, the three-level model predicts bistability on resonance (orange line), while the two-level model does not (dotted line).

Experimentally we choose a large g/κ of approximately 132.3, where the timescales are long and the phases are very well defined, to extract the phase diagram as a function of Δ . We sweep the drive strength for each chosen detuning and record a trace of time-domain single-shot transmission data for each parameter combination. The results are shown in Figs. 4(c) and 4(d), which depict the three regions traced out on the Δ - η parameter plane and the measured dwell time at half-filling (dotted line), respectively.

The color scale in Fig. 4(c) is obtained from the relative weight of the phase space distribution, while the phase boundaries (points) are obtained from measured time-domain single-shot telegraph transmission data as shown in Figs. 4(e)–4(h) for the range of η at $\Delta = 0$ indicated in Fig. 4(a) with a double arrow. Here we define a threshold (dashed line) as described earlier and monitor if a single phase-switching attempt was successful in crossing this threshold within the measurement time. If the answer is yes, the corresponding η and Δ value pair is assigned to the bistable region boundary. If the answer is no, depending on the measured value (below or above threshold), the parameter combination is assigned to the dim phase or the bright phase. The parameter region where multiple crossings occur is assigned to the bistable region. For each detuning, the detection bandwidth and total measurement time have been optimized for us to be able to determine a sharp phase boundary and to resolve the dwell time over 5 orders of magnitude, as shown in Fig. 4(d).

The raw data in Figs. 4(e)–4(h) reveal an interesting difference between partial phase-switching attempts from the dim state, which are quite frequent, and from the bright state, which are rather rare and typically of smaller amplitude (not visible in the data). This asymmetry is not observed in the simulated quantum-jump trajectories as shown, for example, in Appendix A, and its origin is not clear. However, these data point at an additional stabilization mechanism of the bright phase that might also contribute to the stronger-than-expected scaling towards the thermodynamic limit.

Comparing the theoretical and experimental phase diagrams in Figs. 4(a)–4(c), one can see that the two-level neoclassical model, while reproducing the overall resonancelike dependence on the detuning, fails to capture some of the essential features of the experiment. The three-level theory amends these qualitative differences: (i) While the two-level theory can be exactly shown to be independent of the sign of Δ , the three-level theory introduces an asymmetry due to the detuning Δ_{an} of the third level. (ii) Crucially, the three-level theory exhibits a finite bistability interval on resonance, $\Delta = 0$. This comparison underlines the role of the higher-lying transmon levels in shaping the experimental phase diagram, whereas the $g/\kappa \rightarrow \infty$ thermodynamic limit is robust with regard to the variation in

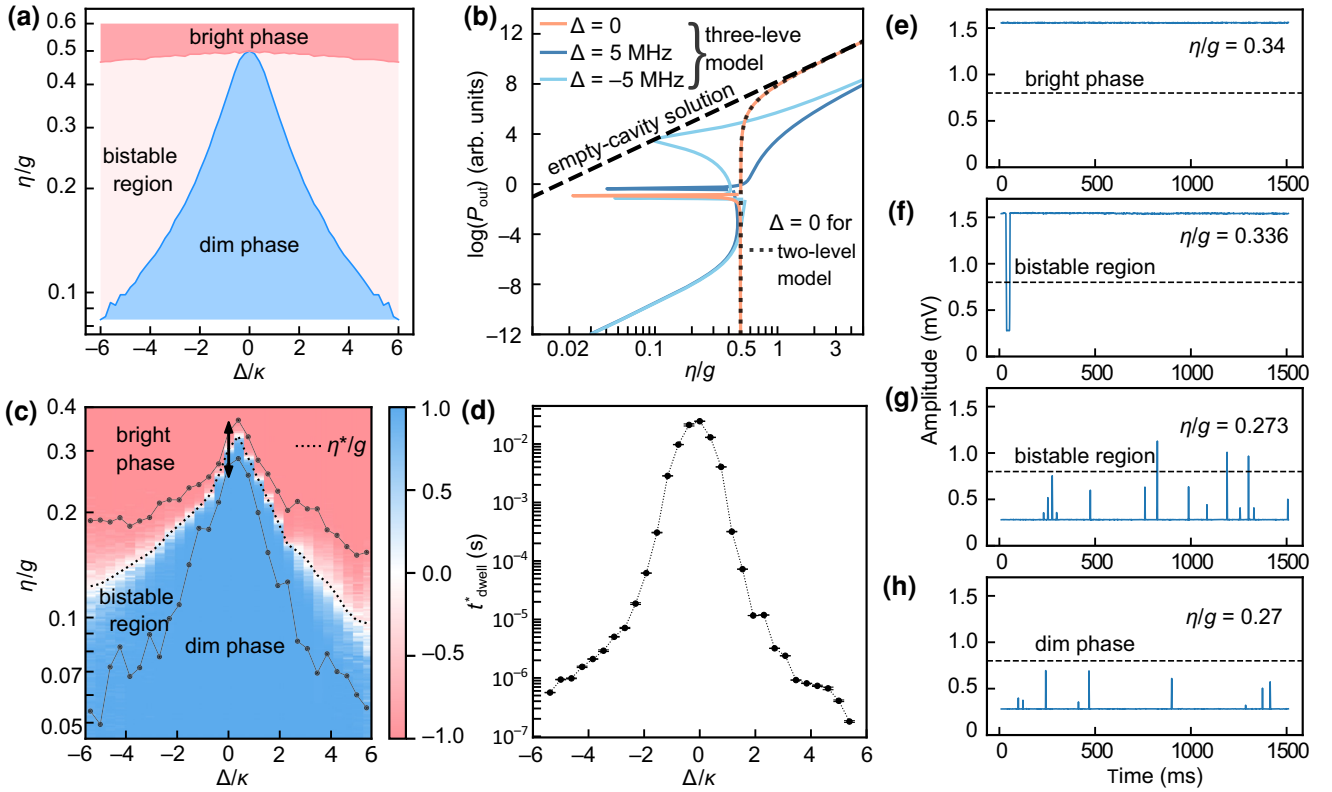


FIG. 4. Photon blockade breakdown phase diagram. (a) Phase diagram on the Δ - η plane obtained from the neoclassical theory for two transmon levels. (b) Typical multistability curves for the transmitted intensity as a function of the drive amplitude obtained from the approximate three-level neoclassical theory detailed in Appendix B. The curves are different for $\Delta = 5$ MHz and $\Delta = -5$ MHz, proving the asymmetry of the phase boundaries. For $\Delta = 0$, the curve obtained from the two-level theory is plotted as a dotted line for comparison, revealing the role of the third level in the appearance of a bistability on resonance. The solution of the three-level theory contains very high order polynomials that lead to numerical problems when the experimental parameters are used. Therefore, here and in (a), model parameters were used: $g_1/\kappa = 30$, $g_2/\kappa = 2.5$, and $\Delta_{\text{an}}/\kappa = -40$ (see Appendix A for the definition of all the parameters of the full model). (c) Experimental PBB phase diagram at $g/\kappa \approx 132$ with boundaries (points) and the half-filling drive strength (dotted line) obtained from the experimental trajectories that exhibit the temporal bistable signal [(e)–(h)]. The color scale of the density plot depicts the ratio $r = (h_1 - h_2)/(h_1 + h_2)$, where h_1 and h_2 are the amplitudes of the peaks of the measured quadrature histograms corresponding to the dim and bright states, respectively; see Figs. 2(d)–2(f). (d) Measured dwell times at half-filling as a function of drive detuning. Error bars are extracted from the mean and standard error of the measured dim and bright dwell times. (e)–(h) Experimentally observed telegraph signals that define the phase boundaries at different η values at $\Delta = 0$ in the range of $\eta/2\pi$ from 85.6 to 115.5 MHz as indicated by a double arrow in (c).

the number of levels as shown by our simulation results above.

VII. DISCUSSION, CONCLUSIONS, AND OUTLOOK

It is important to distinguish the presented PBB phase transition and scaling from several related phenomena. The oldest known such effect is optical bistability, dispersive or absorptive, which is itself a first-order DPT [32,82,83]. In the case of the PBB, we are not in the dispersive regime, however. The driving is close to or on resonance with the bare frequencies of the resonator and the transmon, and the decay of the latter does not play an essential role

either [58]. Another related model is the Duffing oscillator that appears in a circuit QED context as a Kerr nonlinear mode (the transmon) interacting with a linear mode (the resonator) [84,85]. Parametric driving can lead to critical behavior [86], and driven nonlinear inductors have exhibited slow classical switching events triggered by low-frequency thermal fluctuations on the order of seconds [87]. Long bit flip times of up to 100 s have also been observed in a two-photon dissipative oscillator that is characterized by symmetry breaking of the intracavity field phase, but this system does not exhibit a bistability in the photon number [88]. In this respect, the transmon, even with many levels considered, is algebraically very different from a nonlinear oscillator when

it comes to jump operators because these are not bosonic. This results in an essential difference, as verified by our quantum simulations, where it is possible to try the consequences of different algebras. Our simulations clearly rule out the Duffing oscillator model [89], which cannot reproduce the phenomenology of the experiment since its bistable behavior reminiscent of dispersive optical bistability occurs for different parameters and does not exhibit the same scaling towards the thermodynamic limit [90]. Finally, with respect to other recently discovered QPTs and DPTs in the Jaynes-Cummings model or the Rabi model [9,91–93], where thermodynamic limits can also be defined in an abstract way, the difference of PBB as a first-order DPT is that the thermodynamic limit is a strong-coupling limit. The well-resolved discrete spectrum of an interacting bipartite quantum system is essential for the effect.

In this paper, we have experimentally followed the finite-size scaling towards the $g/\kappa \rightarrow \infty$ thermodynamic limit with a characteristic timescale ranging over nearly 7 orders of magnitude. Just like with a finite-size (nonmacroscopic) sample of water, where at 0 °C there is a contest between several metastable and even unstable states instead of true phases of liquid and ice [94], in the PBB bistability for any finite value of g , there is a contest between nonmacroscopically distinct dim and bright states. We have experimentally determined the finite-size scaling exponent of the bistable switching timescale of approximately 5.4 ± 0.2 as well as the scaling exponent of the intracavity photon number of the bright state of approximately 0.95 ± 0.05 . We have also experimentally determined the phase diagram of the PBB phase transition and found that the characteristic dwell times drop by orders of magnitude for finite drive detunings.

We have compared these experimental results with large-scale quantum simulations based on the QJMC method considering different numbers of transmon levels (three, five, and seven) and different dephasing models of higher-lying levels. This comparison indicates that transmon levels up to at least seven play an important role in the dynamics, as does the dephasing, since simulations with dephasing, e.g., due to flux noise, have shown better correspondence to the experimental data. Similarly, the comparison with neoclassical phase diagrams has also underlined the important role of higher transmon levels. The strong-coupling thermodynamic limit is, however, robust with regard to the involvement of the higher-lying states.

While the full quantum simulations reproduce the observed trends correctly, there are significant differences from the experiment in the measured dwell times, which might indicate the presence of further stabilization mechanisms—in particular in the bright attractor—and calls for improved methods to model such strongly coupled multilevel systems.

Even though the computational resources were substantial, the fully quantum numerical simulations were suitable only for modeling the three lowest coupling strengths g/κ investigated. This highlights the need for powerful quantum simulators even in the case of comparably simple circuits and, in particular, to explain how macroscopic phases can be stabilized by individual quantum systems. It is quite surprising that a single transmon qubit can switch back from the bright state—characterized by up to 10^4 intracavity photons—all the way to the dim state and stabilize the empty cavity for seconds in the presence of the continuous large-amplitude coherent input field—in particular given its limited potential confinement [77]. In the future, a fully confined qubit [95] with higher power handling, or larger anharmonicity and superconducting cavities with lower loss could help to explore even more macroscopic phases, pushing the characteristic switching timescales from seconds to days.

Besides its fundamental interest as a quantum-classical phase transition, the PBB bistability also promises a few applications. Since single quantum jumps were shown to trigger the switching from the (nonclassical) dim state to the (closely classical) bright state [58], our system may be considered as a quantum-jump amplifier, where ultimately a macroscopic microwave device (outside the fridge) is getting switched by microscopic quantum events (inside the fridge). An interesting prospect is the control of the switching behavior, which can be envisaged in a parametric way, but preferably with another strongly coupled quantum system. In the latter case, the bistability could act as a quantum readout device with high signal-to-noise ratio. The capability of preparing the system on the verge of a phase-switching event could therefore make it applicable in quantum metrology and sensing based on microwave photon counting [96,97], a new paradigm for the application of first-order DPTs [98–102].

The data and code used to produce the figures in this paper are available online [103].

ACKNOWLEDGMENTS

This work has received funding from the Austrian Science Fund (FWF) through BeyondC (F7105) and the European Union’s Horizon 2020 research and innovation program under Grant Agreement No. 862644 (FETopen QUARTET). A.V. acknowledges support from the National Research, Development and Innovation Office of Hungary (NKFIH) within the Quantum Information National Laboratory of Hungary. The authors thank the MIBA workshop and the Institute of Science and Technology Austria nanofabrication facility for technical support. We are grateful to HUN-REN Cloud for providing us with suitable computational infrastructure for the simulations.

APPENDIX A: THE FULL QUANTUM MODEL

The basic Hamiltonian for a multilevel system interacting with a driven mode reads ($\hbar = 1$)

$$H = \sum_u [h_u |u\rangle \langle u| + i(g_{u+1}a |u+1\rangle \langle u| - \text{h.c.})] + \omega_R a^\dagger a + i(\eta e^{-i\omega t} a^\dagger - \text{h.c.}), \quad (\text{A1})$$

where u indexes the transmon levels, and we assume that only transitions between adjacent levels couple to the mode, with coupling coefficient g_{u+1} . The h_u 's are the bare transmon energies, ω_R is the bare mode frequency, and η and ω are the drive strength and frequency, respectively.

The Hamiltonian is written in the rotating-wave approximation. This is justified as long as the coupling strength does not reach the Bloch-Siegert regime of ultrastrong coupling, meaning $10g_1 \lesssim \hbar, \omega_R$ [61], which holds for our system. For the coupling coefficients, we use the standard relation for transmons:

$$g_{u+1} = \sqrt{u+1} g_1. \quad (\text{A2})$$

For a comprehensive theory of the transmon, see Refs. [104,105].

Transforming to the frame rotating with ω , we obtain a time-independent Hamiltonian with $\Delta \equiv \omega - \omega_R$:

$$H = \sum_u [(h_u - u\omega) |u\rangle \langle u| + i(g_{u+1}a |u+1\rangle \langle u| - \text{H.c.})] - \Delta a^\dagger a + i(\eta a^\dagger - \text{h.c.}). \quad (\text{A3})$$

Here, putting $h_0 = 0$, and assuming the 0-1 transition is resonant with the mode ($h_1 = \omega_R$), we obtain a simple form for the bare transmon Hamiltonian, which we give for the first three levels:

$$H_{\text{transmon}} = -\Delta |1\rangle \langle 1| - (2\Delta - \Delta_{\text{an}}) |2\rangle \langle 2| + \text{contribution of higher levels}, \quad (\text{A4})$$

where $\Delta_{\text{an}} \equiv h_2 - 2h_1$ is the anharmonicity of the third level, which is related to the charging energy.

We turn now to dissipation, which we describe with the Liouvillian

$$\mathcal{L}\rho = \sum_i \left(L_i \rho L_i^\dagger - \frac{1}{2} \{ L_i^\dagger L_i \rho \} \right) \equiv (\mathcal{L}_{\text{mode}} + \mathcal{L}_{\text{relax}} + \mathcal{L}_{\text{dephase}}) \rho \quad (\text{A5})$$

with the following three dissipative channels:

- (1) Resonator decay, $\mathcal{L}_{\text{mode}}$. This is described by the jump operators $L_- = \sqrt{2(n_{\text{th}} + 1)} \kappa a$ and $L_+ =$

$\sqrt{2n_{\text{th}} \kappa} a^\dagger$. Here n_{th} is the number of thermal photons, which can be ignored in our system, so the second kind of quantum jump (absorption of thermal photons) does not exist.

- (2) Energy relaxation of the transmon, $\mathcal{L}_{\text{relax}}$. In analogy with the coupling to the resonator mode, we assume that this occurs only as transitions between adjacent levels. It is described by the jump operator $L_{u+1 \rightarrow u} = \sqrt{\gamma_{u+1 \rightarrow u}} |u\rangle \langle u+1|$. In the simulation, we take $\gamma_{u+1 \rightarrow u}$ equal for all levels, and we identify it with γ_1 in circuit QED.
- (3) Dephasing of the transmon, $\mathcal{L}_{\text{dephase}}$. This is also defined separately for all transmon levels, and its jump operator for level v is

$$L_{\phi,v} = \sqrt{\gamma_{\phi,v}} \left(\sum_{u \neq v} |u\rangle \langle u| - |v\rangle \langle v| \right) = \sqrt{\gamma_{\phi,v}} (\mathbf{1} - 2|v\rangle \langle v|), \quad (\text{A6})$$

so it simply flips the phase of level v by π . Modeling the behavior of the dephasing for different transmon levels is nontrivial. We consider three possibilities:

- (i) $\gamma_{\phi,v} = 0$ for all v . This is only to get a theoretical baseline of dephasing-free behavior.
- (ii) Linear growth as $\gamma_{\phi,v} = v\gamma_\phi/8$ following the above convention, as expected for flux noise due to the higher flux gradient of higher levels. Here the dephasing of the first qubit transition $\gamma_\phi/2\pi = 50$ kHz is taken from the measured vacuum Rabi linewidths and the independently measured cavity linewidth κ .
- (iii) Dephasing proportional to the charge dispersion of the transmon levels [69].

Example trajectories for the three possibilities are displayed in Fig. 5. It is apparent that the third model leads to very noisy trajectories that do not reproduce qualitatively the experimentally observed behavior of stabilized attractors. Therefore, we omitted this possibility from the quantitative comparison presented in the main text.

In the simulation, for each physical parameter set, several trajectories are run with different random number generator seeds. Relying on the assumption of ergodicity, we concatenated these trajectories for a single long trajectory for each parameter set, which is then used for dwell-time statistics. Since each trajectory is started from the ground state, this method has a bias towards the dim state (breaching of ergodicity), which is stronger, the longer the dwell time with respect to the simulation time.

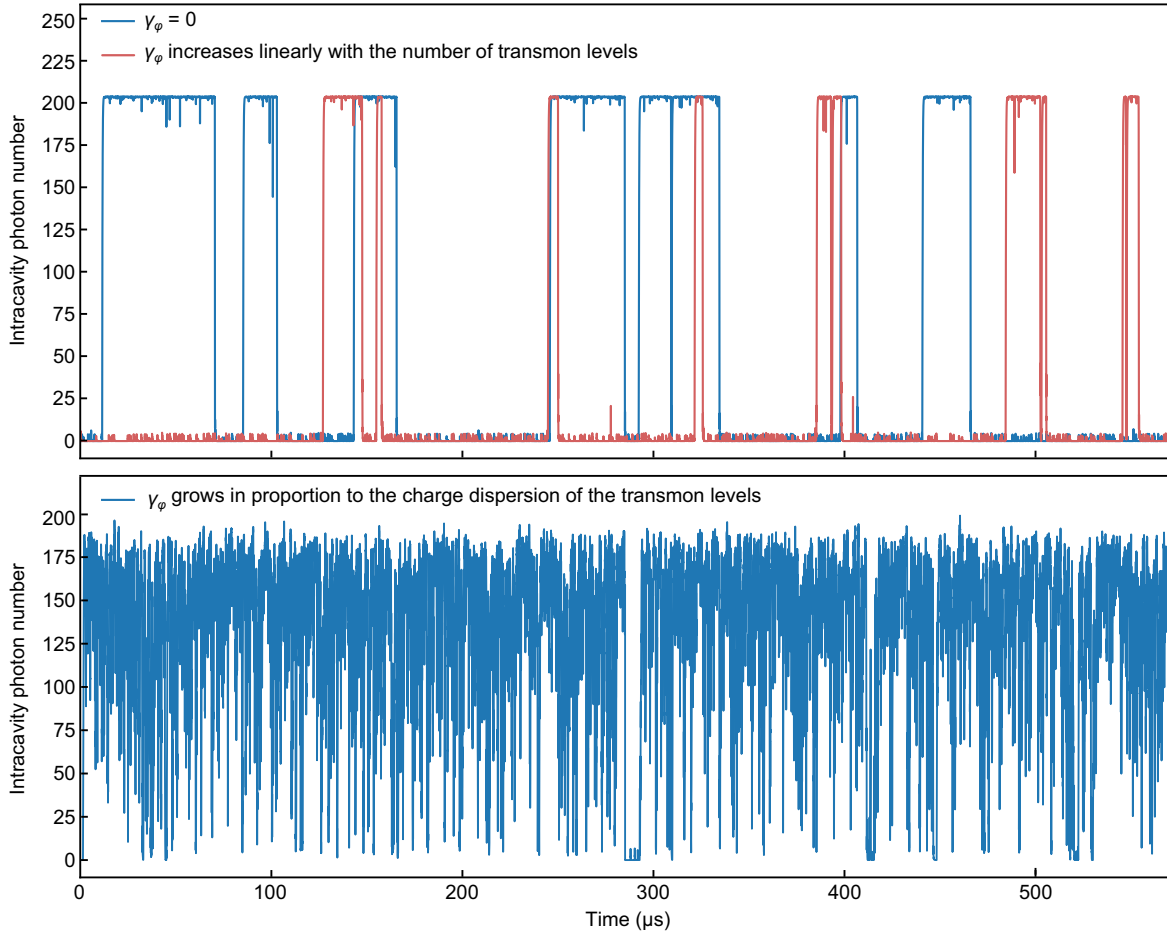


FIG. 5. Simulated example trajectories for the three possibilities of modeling dephasing of higher transmon levels for otherwise identical parameters (five transmon levels, $\gamma_1 = 0$, $\gamma_{\phi,1}/2\pi = 50$ kHz, $\eta/2\pi = 100$ MHz, and $\kappa/2\pi = 14.3$ MHz): no dephasing (top, blue), flux noise model (top, red), and charge dispersion model (bottom, blue). The last case leads to qualitatively incompatible results with very large noise levels and only partially stabilized attractors.

The full quantum simulations were implemented within the C++QED simulation framework [106] and took about 1 year on a 64-core virtual cluster defined within an OpenStack cloud environment [107].

APPENDIX B: AN APPROXIMATE THREE-LEVEL NEOCLASSICAL THEORY AND ITS SOLUTION FOR THE INTENSITY

From the master equation $\dot{\rho} = [H, \rho]/(i\hbar) + \mathcal{L}\rho$ we can derive equations for the expectation values of the operators a and $\sigma_{uv} = |u\rangle\langle v|$, where u and v index atomic levels. In the case of a two-level system, this simply reproduces the Maxwell-Bloch equations, with the added complication of the qubit dephasing. Here, we list the equations for a three-level transmon with states $|g\rangle$, $|e\rangle$, and $|f\rangle$, which still leads to an algebraically tractable scheme. In this case,

six equations are needed for a complete system:

$$\dot{\alpha} = (i\Delta - \kappa)\alpha + \eta - g_1 s_{ge} - g_2 s_{ef}, \quad (\text{B1a})$$

$$\dot{s}_{ge} = (i\Delta - \gamma_1) s_{ge} - g_1 (s_{ee} - s_{gg})\alpha - g_2 s_{gf} \alpha^*, \quad (\text{B1b})$$

$$\dot{s}_{gg} = \gamma_1 s_{ee} - 2g_1 \text{Re} \{ \alpha^* s_{ge} \}, \quad (\text{B1c})$$

$$\begin{aligned} \dot{s}_{ef} = & (i[\Delta - \Delta_{\text{an}}] - [\gamma_1 + 4(\gamma_{\phi,1} + \gamma_{\phi,2})]) s_{ef} \\ & + g_2 (s_{ee} - s_{ff})\alpha + g_1 \alpha^* s_{gf}, \end{aligned} \quad (\text{B1d})$$

$$\dot{s}_{ee} = 2g_1 \text{Re} \{ \alpha^* s_{ge} \} - 2g_2 \text{Re} \{ \alpha^* s_{ef} \} - \gamma_1 s_{ee} + \gamma_1 s_{ff}, \quad (\text{B1e})$$

$$\begin{aligned} \dot{s}_{gf} = & (i[2\Delta - \Delta_{\text{an}}] - [\gamma_1 + 4\gamma_{\phi,2}]) s_{gf} \\ & - g_1 \alpha s_{ef} + g_2 \alpha s_{ge}, \end{aligned} \quad (\text{B1f})$$

where $\alpha = \langle a \rangle$ and $s_{uv} = \langle \sigma_{uv} \rangle$. The system is completed with the completeness relation $s_{gg} + s_{ee} + s_{ff} = 1$.

In the two-level case, one obtains the neoclassical theory by zeroing all the γ 's, and observing that the resulting set of equations conserves the atomic pseudospin. This conservation law replaces the steady-state equation for the atomic population, which becomes degenerate in the case of vanishing atomic decay. One recovers, therefore, a closed system of equations for the steady-state mode amplitude and atomic polarization.

In the three-level case, the neoclassical condition (conservation of pseudospin) reads

$$s_{gg}^2 + s_{ee}^2 + s_{ff}^2 + 2(|s_{ge}|^2 + |s_{gf}|^2 + |s_{ef}|^2) = 1. \quad (\text{B2})$$

After all the different kinds of γ in Eq. (B1) have been zeroed, this can replace the degenerate steady-state equation (B1c). We get rid of the other problematic equation (B1e) by assuming $s_{ff} = 0$. This leaves us with an *approximate* three-level neoclassical theory of five equations for the five steady-state expectation values: the mode amplitude, the atomic ground-state population, and the three atomic polarizations. We use this theory to demonstrate that the appearance of the third level can yield bistability at resonant driving ($\Delta = 0$), in contrast to the two-level case.

Algebraically, this is an inhomogeneous nonlinear set of equations, which we do not need to fully solve, however. Instead, we can obtain a single implicit equation for only the intensity $|\alpha|^2$ as follows. First, we define the complex dispersive shift

$$\Sigma(|\alpha|^2) = -\frac{g_1 s_{ge} + g_2 s_{ef}}{\alpha}. \quad (\text{B3})$$

Then, from Eq. (B1a), we express the steady-state α explicitly. As we show below, Σ depends only on powers of $|\alpha|^2$ and not on other combinations of α and α^* . Therefore, the equation for the intensity can be written as

$$|\alpha|^2 = \frac{|\eta|^2}{|\Sigma(|\alpha|^2) + (i\Delta - \kappa)|^2}. \quad (\text{B4})$$

What we have to show for the validity of Eq. (B4) is that the solutions of s_{ge} and s_{ef} have the form of an $|\alpha|^2$ -dependent expression multiplied by α . The polarizations can be expressed as functions of the population s_{gg} multiplied by α from Eqs. (B1b), (B1d), and (B1f) in the steady state. When these solutions are substituted into the neoclassical condition (B2), the factor α in the solutions becomes $|\alpha|^2$. Hence, s_{gg} can be expressed from this equation as a function of only the intensity, and when this is substituted back into the solutions of the polarizations, we obtain the necessary form for them.

Equation (B4) can be solved numerically. Typical solutions exhibiting bistability at resonance and asymmetry with respect to the sign of Δ are displayed in Fig. 4(b). The

two-level neoclassical theory can be recovered by setting either $g_2 = 0$ or $\Delta_{\text{an}} = 0$.

-
- [1] M. Vojta, Quantum phase transitions, *Rep. Progr. Phys.* **66**, 2069 (2003).
 - [2] L. Capriotti, A. Cuccoli, A. Fubini, V. Tognetti, and R. Vaia, Dissipation-driven phase transition in two-dimensional Josephson arrays, *Phys. Rev. Lett.* **94**, 157001 (2005).
 - [3] S. Diehl, A. Micheli, A. Kantian, B. Kraus, H. Büchler, and P. Zoller, Quantum states and phases in driven open quantum systems with cold atoms, *Nat. Phys.* **4**, 878 (2008).
 - [4] D. Nagy, G. Kónya, G. Szirmai, and P. Domokos, Dicke-model phase transition in the quantum motion of a Bose-Einstein condensate in an optical cavity, *Phys. Rev. Lett.* **104**, 130401 (2010).
 - [5] S. Diehl, A. Tomadin, A. Micheli, R. Fazio, and P. Zoller, Dynamical phase transitions and instabilities in open atomic many-body systems, *Phys. Rev. Lett.* **105**, 015702 (2010).
 - [6] E. M. Kessler, G. Giedke, A. Imamoglu, S. F. Yelin, M. D. Lukin, and J. I. Cirac, Dissipative phase transition in a central spin system, *Phys. Rev. A* **86**, 012116 (2012).
 - [7] A. Le Boité, G. Orso, and C. Ciuti, Steady-state phases and tunneling-induced instabilities in the driven dissipative Bose-Hubbard model, *Phys. Rev. Lett.* **110**, 233601 (2013).
 - [8] F. Minganti, A. Biella, N. Bartolo, and C. Ciuti, Spectral theory of Liouvillians for dissipative phase transitions, *Phys. Rev. A* **98**, 042118 (2018).
 - [9] M.-J. Hwang, P. Rabl, and M. B. Plenio, Dissipative phase transition in the open quantum Rabi model, *Phys. Rev. A* **97**, 013825 (2018).
 - [10] R. Gutiérrez-Jáuregui and H. J. Carmichael, Dissipative quantum phase transitions of light in a generalized Jaynes-Cummings-Rabi model, *Phys. Rev. A* **98**, 023804 (2018).
 - [11] F. Reiter, T. L. Nguyen, J. P. Home, and S. F. Yelin, Cooperative breakdown of the oscillator blockade in the Dicke model, *Phys. Rev. Lett.* **125**, 233602 (2020).
 - [12] M. Soriente, T. L. Heugel, K. Arimitsu, R. Chitra, and O. Zilberberg, Distinctive class of dissipation-induced phase transitions and their universal characteristics, *Phys. Rev. Res.* **3**, 023100 (2021).
 - [13] K. Baumann, C. Guerlin, F. Brennecke, and T. Esslinger, Dicke quantum phase transition with a superfluid gas in an optical cavity, *Nature* **464**, 1301 (2010).
 - [14] F. Verstraete, M. M. Wolf, and J. Ignacio Cirac, Quantum computation and quantum-state engineering driven by dissipation, *Nat. Phys.* **5**, 633 (2009).
 - [15] S. Fernández-Lorenzo and D. Porras, Quantum sensing close to a dissipative phase transition: Symmetry breaking and criticality as metrological resources, *Phys. Rev. A* **96**, 013817 (2017).
 - [16] M. Fitzpatrick, N. M. Sundaresan, A. C. Y. Li, J. Koch, and A. A. Houck, Observation of a dissipative phase transition in a one-dimensional circuit QED lattice, *Phys. Rev. X* **7**, 011016 (2017).

- [17] L. Garbe, M. Bina, A. Keller, M. G. Paris, and S. Felicetti, Critical quantum metrology with a finite-component quantum phase transition, *Phys. Rev. Lett.* **124**, 120504 (2020).
- [18] That is, barring special cases of reducible quantum dynamical semigroups; see D. Nigro, On the uniqueness of the steady-state solution of the Lindblad–Gorini–Kossakowski–Sudarshan equation, *J. Stat. Mech. Theory Exp.* **2019**, 043202 (2019).
- [19] C. Ates, B. Olmos, J. P. Garrahan, and I. Lesanovsky, Dynamical phases and intermittency of the dissipative quantum Ising model, *Phys. Rev. A* **85**, 043620 (2012).
- [20] M. Marcuzzi, E. Levi, S. Diehl, J. P. Garrahan, and I. Lesanovsky, Universal nonequilibrium properties of dissipative Rydberg gases, *Phys. Rev. Lett.* **113**, 210401 (2014).
- [21] V. R. Overbeck, M. F. Maghrebi, A. V. Gorshkov, and H. Weimer, Multicritical behavior in dissipative Ising models, *Phys. Rev. A* **95**, 042133 (2017).
- [22] D. Roscher, S. Diehl, and M. Buchhold, Phenomenology of first-order dark-state phase transitions, *Phys. Rev. A* **98**, 062117 (2018).
- [23] R. Samajdar, W. W. Ho, H. Pichler, M. D. Lukin, and S. Sachdev, Quantum phases of Rydberg atoms on a kagome lattice, *Proc. Natl. Acad. Sci.* **118**, e2015785118 (2021).
- [24] N. E. Myerson-Jain, S. Yan, D. Weld, and C. Xu, Construction of fractal order and phase transition with Rydberg atoms, *Phys. Rev. Lett.* **128**, 017601 (2022).
- [25] C. Carr, R. Ritter, C. G. Wade, C. S. Adams, and K. J. Weatherill, Nonequilibrium phase transition in a dilute Rydberg ensemble, *Phys. Rev. Lett.* **111**, 113901 (2013).
- [26] N. Malossi, M. M. Valado, S. Scotto, P. Huillery, P. Pillet, D. Ciampini, E. Arimondo, and O. Morsch, Full counting statistics and phase diagram of a dissipative Rydberg gas, *Phys. Rev. Lett.* **113**, 023006 (2014).
- [27] F. Letscher, O. Thomas, T. Niederprüm, M. Fleischhauer, and H. Ott, Bistability versus metastability in driven dissipative Rydberg gases, *Phys. Rev. X* **7**, 021020 (2017).
- [28] R. Labouvie, B. Santra, S. Heun, and H. Ott, Bistability in a driven-dissipative superfluid, *Phys. Rev. Lett.* **116**, 235302 (2016).
- [29] F. Ferri, R. Rosa-Medina, F. Finger, N. Dogra, M. Soriente, O. Zilberberg, T. Donner, and T. Esslinger, Emerging dissipative phases in a superradiant quantum gas with tunable decay, *Phys. Rev. X* **11**, 041046 (2021).
- [30] J. Gelhausen and M. Buchhold, Dissipative Dicke model with collective atomic decay: Bistability, noise-driven activation, and the nonthermal first-order superradiance transition, *Phys. Rev. A* **97**, 023807 (2018).
- [31] K. C. Stitely, A. Giraldo, B. Krauskopf, and S. Parkins, Nonlinear semiclassical dynamics of the unbalanced, open Dicke model, *Phys. Rev. Res.* **2**, 033131 (2020).
- [32] W. Casteels, R. Fazio, and C. Ciuti, Critical dynamical properties of a first-order dissipative phase transition, *Phys. Rev. A* **95**, 012128 (2017).
- [33] K. Debnath, E. Mascarenhas, and V. Savona, Nonequilibrium photonic transport and phase transition in an array of optical cavities, *New J. Phys.* **19**, 115006 (2017).
- [34] S. R. K. Rodriguez, W. Casteels, F. Storme, N. Carlon Zambon, I. Sagnes, L. Le Gratiet, E. Galopin, A. Lemaître, A. Amo, C. Ciuti, and J. Bloch, Probing a dissipative phase transition via dynamical optical hysteresis, *Phys. Rev. Lett.* **118**, 247402 (2017).
- [35] V. Savona, Spontaneous symmetry breaking in a quadratically driven nonlinear photonic lattice, *Phys. Rev. A* **96**, 033826 (2017).
- [36] T. Fink, A. Schade, S. Höfling, C. Schneider, and A. Imamoglu, Signatures of a dissipative phase transition in photon correlation measurements, *Nat. Phys.* **14**, 365 (2018).
- [37] F. Vicentini, F. Minganti, R. Rota, G. Orso, and C. Ciuti, Critical slowing down in driven-dissipative Bose-Hubbard lattices, *Phys. Rev. A* **97**, 013853 (2018).
- [38] J. Lang, D. Chang, and F. Piazza, Interaction-induced transparency for strong-coupling polaritons, *Phys. Rev. Lett.* **125**, 133604 (2020).
- [39] Z. Li, F. Claude, T. Boulier, E. Giacobino, Q. Glorieux, A. Bramati, and C. Ciuti, Dissipative phase transition with driving-controlled spatial dimension and diffusive boundary conditions, *Phys. Rev. Lett.* **128**, 093601 (2022).
- [40] R. Hanai, A. Edelman, Y. Ohashi, and P. B. Littlewood, Non-Hermitian phase transition from a polariton Bose-Einstein condensate to a photon laser, *Phys. Rev. Lett.* **122**, 185301 (2019).
- [41] G. Dagvadorj, M. Kulczykowski, M. H. Szymańska, and M. Matuszewski, First-order dissipative phase transition in an exciton-polariton condensate, *Phys. Rev. B* **104**, 165301 (2021).
- [42] T. K. Mavrogordatos, G. Tancredi, M. Elliott, M. J. Peterer, A. Patterson, J. Rahamim, P. J. Leek, E. Ginossar, and M. H. Szymańska, Simultaneous bistability of a qubit and resonator in circuit quantum electrodynamics, *Phys. Rev. Lett.* **118**, 040402 (2017).
- [43] J. M. Fink, A. Dombi, A. Vukics, A. Wallraff, and P. Domokos, Observation of the photon-blockade breakdown phase transition, *Phys. Rev. X* **7**, 011012 (2017).
- [44] P. Brookes, G. Tancredi, A. D. Patterson, J. Rahamim, M. Esposito, T. K. Mavrogordatos, P. J. Leek, E. Ginossar, and M. H. Szymanska, Critical slowing down in circuit quantum electrodynamics, *Sci. Adv.* **7**, eabe9492 (2021).
- [45] G. Beaulieu, F. Minganti, S. Frasca, V. Savona, S. Felicetti, R. Di Candia, and P. Scarlino, Observation of first- and second-order dissipative phase transitions in a two-photon driven Kerr resonator, Preprint [ArXiv:2310.13636](https://arxiv.org/abs/2310.13636) (2023).
- [46] S. Haroche and J.-M. Raimond, *Exploring the Quantum: Atoms, Cavities, and Photons*, Oxford Graduate Texts (Oxford University Press, Oxford, 2006).
- [47] M. Brune, F. Schmidt-Kaler, A. Maali, J. Dreyer, E. Hagley, J. Raimond, and S. Haroche, Quantum Rabi oscillation: A direct test of field quantization in a cavity, *Phys. Rev. Lett.* **76**, 1800 (1996).
- [48] J. M. Fink, M. Göppel, M. Baur, R. Bianchetti, P. J. Leek, A. Blais, and A. Wallraff, Climbing the Jaynes–Cummings ladder and observing its \sqrt{n} nonlinearity in a cavity QED system, *Nature* **454**, 315 (2008).
- [49] J. Kasprzak, S. Reitzenstein, E. A. Muljarov, C. Kistner, C. Schneider, M. Strauss, S. Höfling, A. Forchel,

- and W. Langbein, Up on the Jaynes–Cummings ladder of a quantum-dot/microcavity system, *Nat. Mater.* **9**, 304 (2010).
- [50] A. Imamoğlu, H. Schmidt, G. Woods, and M. Deutsch, Strongly interacting photons in a nonlinear cavity, *Phys. Rev. Lett.* **79**, 1467 (1997).
- [51] C. Lang, D. Bozyigit, C. Eichler, L. Steffen, J. M. Fink, A. A. Abdumalikov, M. Baur, S. Filipp, M. P. da Silva, A. Blais, and A. Wallraff, Observation of resonant photon blockade at microwave frequencies using correlation function measurements, *Phys. Rev. Lett.* **106**, 243601 (2011).
- [52] R. Ohira, S. Kume, H. Takahashi, and K. Toyoda, Polariton blockade in the Jaynes–Cummings–Hubbard model with trapped ions, *Quantum Sci. Technol.* **6**, 024015 (2021).
- [53] H. J. Carmichael, Breakdown of photon blockade: A dissipative quantum phase transition in zero dimensions, *Phys. Rev. X* **5**, 031028 (2015).
- [54] A. Dombi, A. Vukics, and P. Domokos, Bistability effect in the extreme strong coupling regime of the Jaynes–Cummings model, *Eur. Phys. J. D* **69**, 60 (2015).
- [55] J. B. Curtis, I. Boettcher, J. T. Young, M. F. Maghrebi, H. Carmichael, A. V. Gorshkov, and M. Foss-Feig, Critical theory for the breakdown of photon blockade, *Phys. Rev. Res.* **3**, 023062 (2021).
- [56] I. Chiorescu, N. Groll, S. Bertaina, T. Mori, and S. Miyashita, Magnetic strong coupling in a spin-photon system and transition to classical regime, *Phys. Rev. B* **82**, 024413 (2010).
- [57] A. Pályi, P. R. Struck, M. Rudner, K. Flensberg, and G. Burkard, Spin-orbit-induced strong coupling of a single spin to a nanomechanical resonator, *Phys. Rev. Lett.* **108**, 206811 (2012).
- [58] A. Vukics, A. Dombi, J. M. Fink, and P. Domokos, Finite-size scaling of the photon-blockade breakdown dissipative quantum phase transition, *Quantum* **3**, 150 (2019).
- [59] J. Koch, T. M. Yu, J. Gambetta, A. A. Houck, D. I. Schuster, J. Majer, A. Blais, M. H. Devoret, S. M. Girvin, and R. J. Schoelkopf, Charge-insensitive qubit design derived from the Cooper pair box, *Phys. Rev. A* **76**, 042319 (2007).
- [60] H. Paik, D. I. Schuster, L. S. Bishop, G. Kirchmair, G. Catelani, A. P. Sears, B. R. Johnson, M. J. Reagor, L. Frunzio, L. I. Glazman, S. M. Girvin, M. H. Devoret, and R. J. Schoelkopf, Observation of high coherence in Josephson junction qubits measured in a three-dimensional circuit QED architecture, *Phys. Rev. Lett.* **107**, 240501 (2011).
- [61] P. Forn-Díaz, L. Lamata, E. Rico, J. Kono, and E. Solano, Ultrastrong coupling regimes of light-matter interaction, *Rev. Mod. Phys.* **91**, 025005 (2019).
- [62] A. P. Sears, A. Petrenko, G. Catelani, L. Sun, H. Paik, G. Kirchmair, L. Frunzio, L. I. Glazman, S. M. Girvin, and R. J. Schoelkopf, Photon shot noise dephasing in the strong-dispersive limit of circuit QED, *Phys. Rev. B* **86**, 180504 (2012).
- [63] C. W. Gardiner and M. J. Collett, Input and output in damped quantum systems: Quantum stochastic differential equations and the master equation, *Phys. Rev. A* **31**, 3761 (1985).
- [64] A. A. Houck, J. A. Schreier, B. R. Johnson, J. M. Chow, J. Koch, J. M. Gambetta, D. I. Schuster, L. Frunzio, M. H. Devoret, S. M. Girvin, and R. J. Schoelkopf, Controlling the spontaneous emission of a superconducting transmon qubit, *Phys. Rev. Lett.* **101**, 080502 (2008).
- [65] C. Savage and H. Carmichael, Single atom optical bistability, *IEEE J. Quantum. Electron.* **24**, 1495 (1988).
- [66] P. Alsing and H. Carmichael, Spontaneous dressed-state polarization of a coupled atom and cavity mode, *Quantum Opt.: J. Eur. Opt. Soc. B* **3**, 13 (1991).
- [67] M. A. Armen, A. E. Miller, and H. Mabuchi, Spontaneous dressed-state polarization in the strong driving regime of cavity QED, *Phys. Rev. Lett.* **103**, 173601 (2009).
- [68] M. Delanty, S. Rebić, and J. Twamley, Superradiance and phase multistability in circuit quantum electrodynamics, *New J. Phys.* **13**, 053032 (2011).
- [69] L. S. Bishop, J. M. Chow, J. Koch, A. A. Houck, M. H. Devoret, E. Thuneberg, S. M. Girvin, and R. J. Schoelkopf, Nonlinear response of the vacuum Rabi resonance, *Nat. Phys.* **5**, 105 (2009).
- [70] J. M. Fink, L. Steffen, P. Studer, L. S. Bishop, M. Baur, R. Bianchetti, D. Bozyigit, C. Lang, S. Filipp, P. J. Leek, and A. Wallraff, Quantum-to-classical transition in cavity quantum electrodynamics, *Phys. Rev. Lett.* **105**, 163601 (2010).
- [71] Note that a measurement of the bistable signal in the time domain gives additional information compared with observing the hysteresis cycle by sweeping a parameter of the drive [amplitude or detuning; see Figs. 2(g) and 4(c)]. This is because the former also tells us about the timescale on which we can expect the hysteresis to manifest itself. If we sweep the drive amplitude over the bistability domain faster than the dwell time, then we observe perfect hysteresis. However, the sweep should not be too fast, so as to avoid provoking a switch between the attractors, which can be expected by nonadiabatic changes of parameters. In contrast, if the timescale of the sweep is slower than the dwell time, we would observe several switches between the attractors while sweeping the drive amplitude over the bistability domain.
- [72] A. Vukics, C++QEDv2: The multi-array concept and compile-time algorithms in the definition of composite quantum systems, *Comput. Phys. Commun.* **183**, 1381 (2012).
- [73] M. Korniyik and A. Vukics, The Monte Carlo wavefunction method: A robust adaptive algorithm and a study in convergence, *Comput. Phys. Commun.* **238**, 88 (2019).
- [74] I. Pietikäinen, S. Danilin, K. Kumar, J. Tuorila, and G. Paraoanu, Multilevel effects in a driven generalized Rabi model, *J. Low. Temp. Phys.* **191**, 354 (2018).
- [75] H.-P. Breuer and F. Petruccione, *The Theory of Open Quantum Systems* (Oxford University Press, New York, 2007).
- [76] F. Beaudoin, J. M. Gambetta, and A. Blais, Dissipation and ultrastrong coupling in circuit QED, *Phys. Rev. A* **84**, 043832 (2011).
- [77] R. Shillito, A. Petrescu, J. Cohen, J. Beall, M. Hauru, M. Ganahl, A. G. M. Lewis, G. Vidal, and A. Blais,

- Dynamics of transmon ionization, *Phys. Rev. Appl.* **18**, 034031 (2022).
- [78] M. Zemlicka, E. Redchenko, M. Peruzzo, F. Hassani, A. Trioni, S. Barzanjeh, and J. M. Fink, Compact vacuum gap transmon qubits: Selective and sensitive probes for superconductor surface losses, *Phys. Rev. Appl.* **20**, 044054 (2023).
- [79] W. Nagourney, J. Sandberg, and H. Dehmelt, Shelved optical electron amplifier: Observation of quantum jumps, *Phys. Rev. Lett.* **56**, 2797 (1986).
- [80] J. C. Bergquist, R. G. Hulet, W. M. Itano, and D. J. Wineland, Observation of quantum jumps in a single atom, *Phys. Rev. Lett.* **57**, 1699 (1986).
- [81] Á. Kurkó, N. Német, and A. Vukics, Is the photon-blockade breakdown a quantum effect? a neoclassical story, Preprint [ArXiv:2310.08388](https://arxiv.org/abs/2310.08388) (2023).
- [82] P. Drummond and D. Walls, Quantum theory of optical bistability. I. Nonlinear polarisability model, *J. Phys. A: Math. General* **13**, 725 (1980).
- [83] W. Casteels, F. Storme, A. Le Boité, and C. Ciuti, Power laws in the dynamic hysteresis of quantum nonlinear photonic resonators, *Phys. Rev. A* **93**, 033824 (2016).
- [84] S. Rebić, J. Twamley, and G. J. Milburn, Giant Kerr nonlinearities in circuit quantum electrodynamics, *Phys. Rev. Lett.* **103**, 150503 (2009).
- [85] V. Peano and M. Thorwart, Dynamical bistability in the driven circuit QED, *EPL (Europhys. Lett.)* **89**, 17008 (2010).
- [86] W. Wustmann and V. Shumeiko, Parametric effects in circuit quantum electrodynamics, *Low Temp. Phys.* **45**, 848 (2019).
- [87] P. R. Muppalla, O. Gargiulo, S. I. Mirzaei, B. P. Venkatesh, M. L. Juan, L. Grünhaupt, I. M. Pop, and G. Kirchmair, Bistability in a mesoscopic Josephson junction array resonator, *Phys. Rev. B* **97**, 024518 (2018).
- [88] C. Berdou, *et al.*, One hundred second bit-flip time in a two-photon dissipative oscillator, *PRX Quantum* **4**, 020350 (2023).
- [89] M. Dykman, *Fluctuating Nonlinear Oscillators: From Nanomechanics to Quantum Superconducting Circuits* (Oxford University Press, Oxford, 2012).
- [90] It is straightforward to show that in a mean-field treatment of a linear oscillator (the resonator) coupled to a Duffing oscillator (the transmon), the former can be eliminated from the dynamics, leading to a single Duffing oscillator with rescaled parameters but with the Kerr term unaffected. This shows that the nonlinearity of the model is independent of the coupling strength, in sharp contrast to the PBB, where the nonlinearity increases with g , which is the basis of the strong coupling thermodynamic limit. See also Qi-Ming Chen, *et al.* Quantum behavior of the Duffing oscillator at the dissipative phase transition. *Nat. Commun.* **14**, 2896 (2023).
- [91] M.-J. Hwang, R. Puebla, and M. B. Plenio, Quantum phase transition and universal dynamics in the Rabi model, *Phys. Rev. Lett.* **115**, 180404 (2015).
- [92] M.-J. Hwang and M. B. Plenio, Quantum phase transition in the finite Jaynes-Cummings lattice systems, *Phys. Rev. Lett.* **117**, 123602 (2016).
- [93] J. Larson and E. K. Irish, Some remarks on “superradiant” phase transitions in light-matter systems, *J. Phys. A: Math. Theor.* **50**, 174002 (2017).
- [94] U. Thiele, T. Frohoff-Hülsmann, S. Engelnkemper, E. Knobloch, and A. J. Archer, First order phase transitions and the thermodynamic limit, *New J. Phys.* **21**, 123021 (2019).
- [95] F. Hassani, M. Peruzzo, L. Kapoor, A. Trioni, M. Zemlicka, and J. M. Fink, Inductively shunted transmons exhibit noise insensitive plasmon states and a fluxon decay exceeding 3 hours, *Nat. Commun.* **14**, 3968 (2023).
- [96] S. Guha and B. I. Erkmen, Gaussian-state quantum-illumination receivers for target detection, *Phys. Rev. A* **80**, 052310 (2009).
- [97] K. Petrovnin, J. Wang, M. Perelshtein, P. Hakonen, and G. S. Paraoanu, Microwave photon detection at parametric criticality, Preprint [ArXiv:2308.07084](https://arxiv.org/abs/2308.07084) (2023).
- [98] S. Fernández-Lorenzo and D. Porras, Quantum sensing close to a dissipative phase transition: Symmetry breaking and criticality as metrological resources, *Phys. Rev. A* **96**, 013817 (2017).
- [99] M. Raghunandan, J. Wrachtrup, and H. Weimer, High-density quantum sensing with dissipative first order transitions, *Phys. Rev. Lett.* **120**, 150501 (2018).
- [100] L.-P. Yang and Z. Jacob, Engineering first-order quantum phase transitions for weak signal detection, *J. Appl. Phys.* **126**, 174502 (2019).
- [101] T. L. Heugel, M. Biondi, O. Zilberberg, and R. Chitra, Quantum transducer using a parametric driven-dissipative phase transition, *Phys. Rev. Lett.* **123**, 173601 (2019).
- [102] R. Di Candia, F. Minganti, K. Petrovnin, G. Paraoanu, and S. Felicetti, Critical parametric quantum sensing, *npj Quantum Inf.* **9**, 23 (2023).
- [103] <https://doi.org/10.5281/zenodo.10518321>.
- [104] A. Blais, A. L. Grimsmo, S. M. Girvin, and A. Wallraff, Circuit quantum electrodynamics, *Rev. Mod. Phys.* **93**, 025005 (2021).
- [105] J. A. Schreier, A. A. Houck, J. Koch, D. I. Schuster, B. R. Johnson, J. M. Chow, J. M. Gambetta, J. Majer, L. Frunzio, M. H. Devoret, S. M. Girvin, and R. J. Schoelkopf, Suppressing charge noise decoherence in superconducting charge qubits, *Phys. Rev. B* **77**, 180502 (2008).
- [106] <http://github.com/vukics/cppqed>.
- [107] <http://science-cloud.hu/>.